J. Space Weather Space Clim. 2024, **14**, 16
© Y. Yokoyama & S. Taguchi, Published by EDP Sciences 2024
https://doi.org/10.1051/swsc/2024013

Available online at:
www.swsc-journal.org

RESEARCH ARTICLE OPEN ACCESS

The nature of the mesoscale field-aligned currents in the auroral oval for positive IMF B_Z: More frequent occurrence in the dawnside sector than in the duskside sector

Yoshihiro Yokoyama[1,*] and Satoshi Taguchi[2]

[1] Swedish Institute of Space Physics, Bengt Hultqvists väg 1, 981 92 Kiruna, Sweden
[2] Department of Geophysics, Graduate School of Science, Kyoto University, Kyoto 6068502, Japan

Received 15 October 2023 / Accepted 12 April 2024

Abstract – To understand the similarities and differences between the duskside mesoscale quasistatic field-aligned currents (FACs) and the dawnside mesoscale FACs, we examined the magnetic field data obtained through the constellation measurements of Swarm satellites for a four-year period. The automatic event identification method developed in the previous study (Yokoyama Y et al., 2021) identified events of quasistatic mesoscale FACs, which are embedded in the diminished dawnside and duskside Region 1/2 current systems, in 774 passes out of 4001 passes on the dawnside, and 443 out of 3755 passes on the duskside, respectively. The dawnside and duskside mesoscale FACs have similar occurrence tendencies such that both have a relatively high occurrence ratio for positive IMF B_Z, occur regardless of sunlight conditions, and have the current density increasing with the solar wind proton density. On the other hand, one notable difference was found; the occurrence ratio of the dawnside mesoscale FACs is approximately 1.7 times higher than that of the duskside mesoscale FACs. This difference is discussed in terms of the dawn–dusk asymmetry of the occurrence of Kelvin Helmholtz instabilities on the magnetopause.

Keywords: Field-aligned current / Mesoscale structure / Swarm satellite / Low latitude boundary layer

1 Introduction

Field-aligned currents (FACs) flowing between the polar ionosphere and the magnetosphere are responsible for the transport of energy and momentum between those two regions and are very important phenomena in understanding how both regions interact with each other. Recent multi-satellite observations have shown that magnetic perturbations on horizontal scales longer than 150–200 km are due to the quasistatic field-aligned currents (Gjerloev et al., 2011), which are thought to be associated with the quasistatic interaction between those two regions, the polar ionosphere and the magnetosphere, while magnetic perturbations on horizontal scales of ~10 km or less are due to Alfvén waves (Lühr et al., 2015), which is associated with the dynamic interaction. Magnetic perturbations with horizontal scale sizes in between are expected to be caused by both phenomena.

Recent studies have revealed additional features of the magnetic perturbations with such intermediate horizontal scale sizes found in certain MLT regions. Yokoyama et al. (2020, 2021) have found that in the duskside sector (14–18 MLT auroral oval), several mesoscale magnetic perturbations (each with a latitudinal size of 10 to 40 km), which are embedded in the diminished Region 1/Region 2 current system, are caused by the quasistatic FACs, and that those are prominent when IMF has a northward component. Yokoyama et al. (2020) have also shown that this type of the mesoscale FAC flows along the magnetic field lines connecting to the low-latitude boundary plasma (LLBL). In Yokoyama et al. (2021), the generation of that mesoscale FAC has been discussed; they argued that the deceleration of the tailward flow in the LLBL, which is formed by reconnection that occurs twice in succession (Borgogno et al., 2015), is responsible for the generation of the mesoscale FAC on the closed field lines in the duskside LLBL.

The LLBL is present on both the dawnside and duskside flanks of the magnetosphere. Since the mechanism proposed by Yokoyama is not limited only to the duskside LLBL, the mesoscale FACs with similar characteristics are expected to flow in the dawnside sector as well. The purpose of this study is to clarify whether the mesoscale FACs having characteristics similar to the ones with the duskside mesoscale FACs are also identified in the dawnside sector. Swarm satellites cover all

*Corresponding author: yokoyama@irf.se

magnetic local times in about 130–140 days. By examining data acquired by Swarm satellites over a period of time sufficiently longer than those periods, it is possible to identify the mesoscale FACs from a sufficient number of satellite passes both in the duskside sector and dawnside sector. We examined the magnetic field data obtained through the constellation measurements of Swarm satellites for a four-year period to understand the similarities and differences between the duskside mesoscale FACs and the dawnside mesoscale FACs. We apply the automatic event identification method used in Yokoyama et al. (2021) to magnetic field data acquired by multiple Swarm satellites crossing the high-latitude part of the auroral oval.

2. Materials and methods

2.1 Data

The Swarm constellation mission consists of three identical near-polar orbiting satellites A, B, and C launched by the European Space Agency (ESA) on November 22, 2013; each of the three satellites carries the fluxgate magnetometer to measure the magnetic field vector (Friis-Christensen et al., 2006). In this study, we analyzed the east–west component of the magnetic perturbations (1 Hz resolution) after subtracting the International Geomagnetic Reference Field (IGRF-12, Thébault et al., 2015) from the observed magnetic field, which is coordinate converted in North–East–Center local Cartesian coordinates (Olsen et al., 2013).

Of the three satellites, Swarm-A and Swarm-C (hereafter referred to as SW-A and SW-C, respectively) have been flying side by side, separated by 1.4° in longitude at an altitude of about 460 km with a slight time difference (typically 3–10 s) since April 17, 2014 (SW-C ahead of SW-A). This satellite configuration helps us understand if the FACs that cause magnetic disturbances are stable during such a short period of time. In this study, we analyzed data observed by SW-A and SW-C in the northern hemisphere over a period of 4 years, from January 2017 to December 2020. This period slightly overlaps with the period studied by Yokoyama et al. (2021), i.e., May 2014 to May 2017, but is mostly different. The reason for choosing the different period is to see whether the mesoscale FACs in the duskside sector, which have been studied by Yokoyama et al. (2021), are not phenomena limited to the period studied in that paper, i.e., 2014–2017, by examining the duskside mesoscale FACs observed for the different period. We also used current density data provided as the Swarm Level 2 products. The ESA provides two types of current densities, which are calculated using a single spacecraft solution and a dual spacecraft solution (Ritter et al., 2013). We analyzed the former data. For solar wind and IMF, OMNI 1-min data were used.

2.2 Overview of event identification method

The event identification method used in this study is essentially the same as that derived by Yokoyama et al. (2021) for the duskside auroral oval. Four conditions were applied to the automatic event identification: (1) SW-A and SW-C traversed the high-latitude part of the dawnside (or duskside) auroral oval (as mentioned above, this study is also intended to verify the

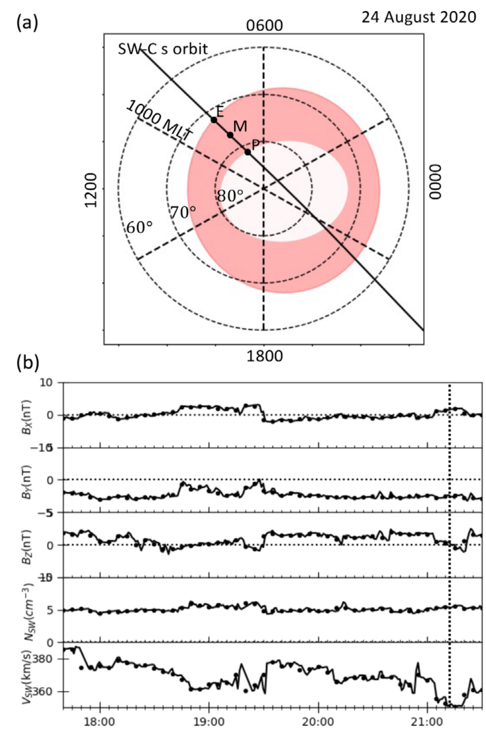

Figure 1. (a) One of the SW-C passes on the MLT-MLAT dial in the magnetic apex coordinates, and corresponding auroral oval (shaded red region), which was calculated from the model by Xiong & Lühr (2014). The point *E* (or *P*) represents the intersection of the orbit and the equatorward (or poleward) boundary of the dawnside part of the auroral oval, and *M* is the middle of their points. (b) IMF and solar wind plasma data from OMNI between 17:40 and 21:30 UT on 24 August, 2020. From top to bottom, the three components of IMF (B_X, B_Y, and B_Z) in GSM coordinate, the solar wind proton density, and flow speed are plotted. The vertical dotted lines at 21:12:02 UT indicate the time when SW-C crossed the point *M*.

generality of the mesoscale FAC observed in the duskside sector); (2) the collocated large-scale Region 1/2 systems are diminished, and the magnetic perturbations produced by the mesoscale FACs are larger than those produced by the diminished large-scale Region 1/2 systems; (3) the mesoscale FACs consist of multiple (at least five upward/downward current) regions; and (4) the mesoscale FACs show quasistatic features.

For Condition 1, we determined the dawnside auroral oval range as 6–10 MLT. The duskside range is the same as that adopted by Yokoyama et al. (2021), i.e., 14–18 MLT. To determine the "high-latitude part" of the auroral oval for each pass, we used the empirical model of the auroral oval developed by Xiong & Lühr (2014). This empirical model provides the poleward and equatorward boundaries of the auroral oval for the input of the 3-h time series of the IMF B_Y, B_Z, and the solar wind speed. Figure 1a shows an example of the auroral oval model together with one of the SW-C orbits. The solid black line indicates the SW-C orbit. The black dot shown as *E* (or *P*) on the line represents the intersection of that orbit and the equatorward (or poleward) boundary of the model auroral oval. The black dot *M* is the middle of these two points. Note that

Condition 1 requires that both M and P should be in 6–10 MLT or 14–18 MLT.

In the 3-h time series for the model input, we used the data of IMF B_Y, B_Z, and the solar wind speed starting from $t = (t_0 - 3.5)$ h to $(t_0 - 0.5)$ h, considering a 30-min time delay, where t_0 is UT when SW-C crosses 70 MLAT. The 30-min delay is consistent with the result by Xiong & Lühr (2014). For the example shown in Figure 1a, t_0 is 21:10 UT. IMF B_X, B_Y, B_Z, the solar wind proton density, and speed during 3 h 50 min on 24 August 2020, which includes the 3-h period from 17:40 to 20:40 UT, are shown in Figure 1b. The solid line and dots in each panel of Figure 1b indicate 1-min OMNI data and its 5-min average, respectively. From top to bottom, the three components of IMF (B_X, B_Y, and B_Z) in the GSM coordinates, solar wind proton density, and flow speed are plotted. The vertical dotted line at 21:12:02 UT indicates the time when SW-C crossed the point M. The IMF B_Z (third panel) was mostly positive during the plotted interval. The average values of IMF B_X, B_Y, and B_Z during 30 min before the time shown the vertical dotted line (21:12:02 UT) are approximately -0.62, -2.2, and 1.7 nT, respectively. The 30-min average proton density and speed were approximately 4.9 cm^{-3} and 380 km s^{-1}, respectively. We used these 30-min average values for statistical analyses.

Next, for the satellite orbits that satisfied Condition 1, we analyzed the magnetic perturbation data along each orbit, and imposed Condition 2 and Condition 3. Condition 2 and Condition 3 are the same as those used in Yokoyama et al. (2021) as Condition 2 and Condition 3, respectively. The detail of Condition 2 is as follows: We first determined the "amplitude" of the large-scale variation as half of the difference between the maximum and minimum values of the low-pass filtered data so that we could estimate the magnitude of the large-scale variations. For the mesoscale variations, we considered the maximum perturbations for each pass. We then took orbits wherein the maximum perturbation of the mesoscale variations is larger than the "amplitude" of the large-scale variation.

As Condition 3, we first considered the local maxima and minima from the mesoscale variations between E and P and then defined each upward/downward FAC region as the region between the point for one local maximum and that for one local minimum. We also calculated the current intensity of each FAC region from the value of the difference between the local maximum and local minimum. We took the passes where five or more mesoscale current regions could be determined with the condition that the region with a current intensity of less than 20% of the maximum current intensity for each pass is ruled out. Note that we are not suggesting that the whole of five or more mesoscale current regions has a scale size of 10–40 km.

As Condition 4, we compared the SW-A data that were shifted by the satellite separation time (typically 3–10 s) and SW-C data, and obtained the average correlation coefficient in each 30 s window for the range between M and P points of SW-C. When the average of the correlation coefficients was higher than 0.6, we regarded the mesoscale magnetic variations as being quasistatic. We found events of quasistatic mesoscale FACs embedded in the diminished dawnside and duskside Region 1/2 current systems in 774 passes out of 4001 passes on the dawnside and 443 out of 3755 passes on the duskside, respectively.

2.3 An example of the quasistatic mesoscale FACs in the dawnside sector

Figure 2 shows an example of the quasistatic mesoscale FACs in the dawnside sector. This event occurred on August 24, 2020. Figure 2a plots the east-west component of the SW-C magnetic perturbation data from 21:10:20 to 21:14:14 UT on 24 August 2022. The three vertical dotted lines indicate the time when SW-C passed E, M, and P in its orbit. Figure 2b is the expanded plot of the mesoscale and large-scale magnetic perturbations from 21:10:50 UT to 21:13:14 UT. In this case, the "amplitudes" of the mesoscale and large-scale magnetic variations are 66.5 nT and 35.4 nT, respectively. The positive and negative gradients of the magnetic perturbations represent FACs flowing into and away from the ionosphere, respectively. Multiple mesoscale FAC regions were observed. SW-C observed 14 upward and downward mesoscale FAC regions between M and P in the orbit. Figures 2c and 2d show the comparison in the region between M and P. In Figure 2c, we superposed the 7 s (separation time of the satellites) shifted SW-A data (red) on the SW-C (blue). The plot in Figure 2d is the correlation coefficient, which shows that the correlation coefficient generally exceeds 0.6. The average correlation coefficient for the entire period is 0.83. As can be seen from this high correlation coefficient, the two magnetic disturbances observed with a 7-s time lag are in good agreement with each other.

3 Results

3.1 Latitudinal size

Figure 3 shows the distribution of latitudinal size of the upward and downward FACs estimated by the method used in Yokoyama et al. (2021). We used current density data available as Swarm Level 2 products for this analysis (also for the analysis for Fig. 6, which is shown later). The left two panels show that the latitudinal size of the dawnside FAC does not usually exceed 40 km. Similar features are seen in the latitudinal size of the duskside FAC (right panels). The result for the duskside sector also agrees well with that obtained by Yokoyama et al. (2020, 2021) for a different period (May 2014 to May 2017).

3.2 Relationship to solar zenith angle

Figure 4 shows the histograms of the solar zenith angles (blue bars) and the occurrence ratio (light-blue lines) for 774 dawnside and 443 duskside events in each 10° bin from 45° to 135° solar zenith angle. We used the solar zenith angle at the midpoint between P and M for each SW-C pass. The occurrence ratios show similar characteristics in both the dawnside and duskside sectors. That is, they are generally 10% over a wide range, although they are somewhat higher in the range of zenith angles from 95° to 115°, where the sunlight is weaker. This result suggests that the low ionospheric conductivity, which occurs for larger solar zenith angles, i.e., in the dark ionosphere, does not play an important role in the generation of the dawnside multiple mesoscale FACs, as was shown for the duskside mesoscale FACs by Yokoyama et al. (2021). The tendency for the duskside sector is also similar to that obtained by Yokoyama et al. (2021) for a different period.

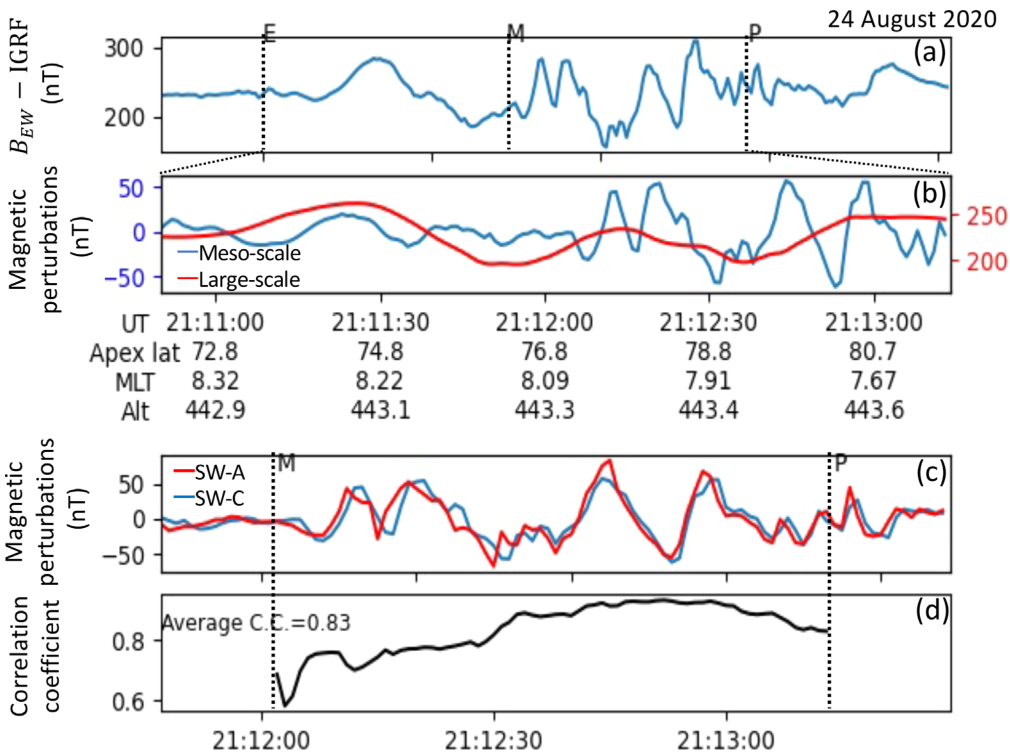

Figure 2. (a) Magnetic perturbations (east–west component) observed by SW-C during 21:10:20–21:14:14 UT on 24 August 2020, (b) Expanded plot of the mesoscale (blue) and large-scale (red) magnetic perturbations, (c) Comparison plot wherein the 7 s shifted SW-A data (red) are superposed on the SW-C data (blue), and (d) Correlation coefficients in each 30 s window between the SW-A and SW-C data for *M* to *P*.

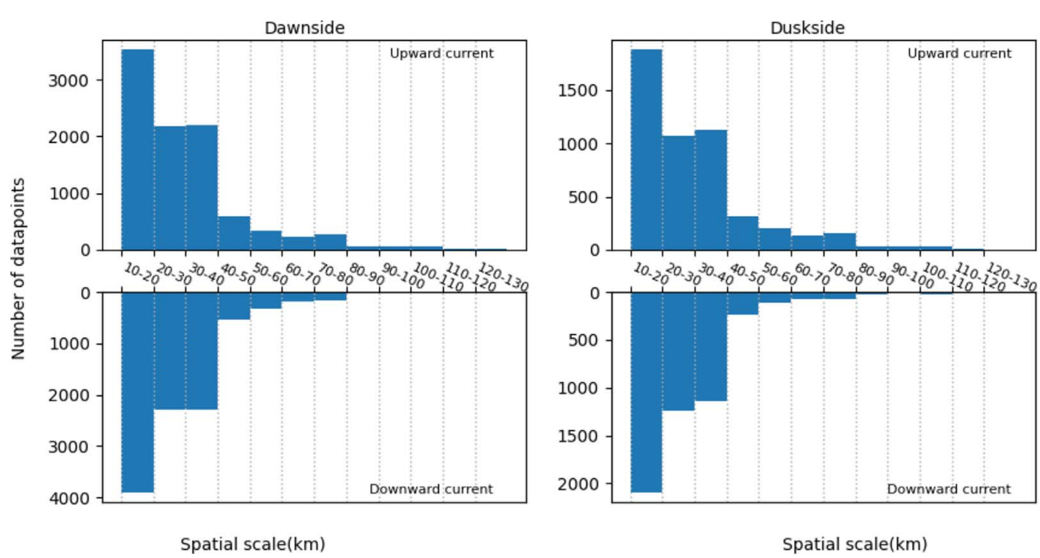

Figure 3. Distribution of the latitudinal size of the upward FAC and downward FAC observed by SW-C in the dawnside sector and the duskside sector. The horizontal axis represents 10-km bins from 10–20 km to 120–130 km.

3.3 Relation to the solar wind parameters

Figures 5a–5c show the relation to the three components of the IMF. The numbers shown in red in each bin of the six panels represent the numbers of Swarm trajectories in that bin, and the number of events relative to this number is shown as the occurrence ratio. We used the IMF values averaged for 30 min immediately before SW-C entry to *M*, as was mentioned above. For the relation for IMF B_X (Fig. 5a), the occurrence ratio in the dawnside sector is roughly 20% ranging from −5 nT to 5 nT, regardless of the B_X value. Similarly, for the duskside sector, the occurrence ratio is relatively constant regardless of the B_X value, and the values are in the range of 10%–15% (average about 12%), indicating that the occurrence

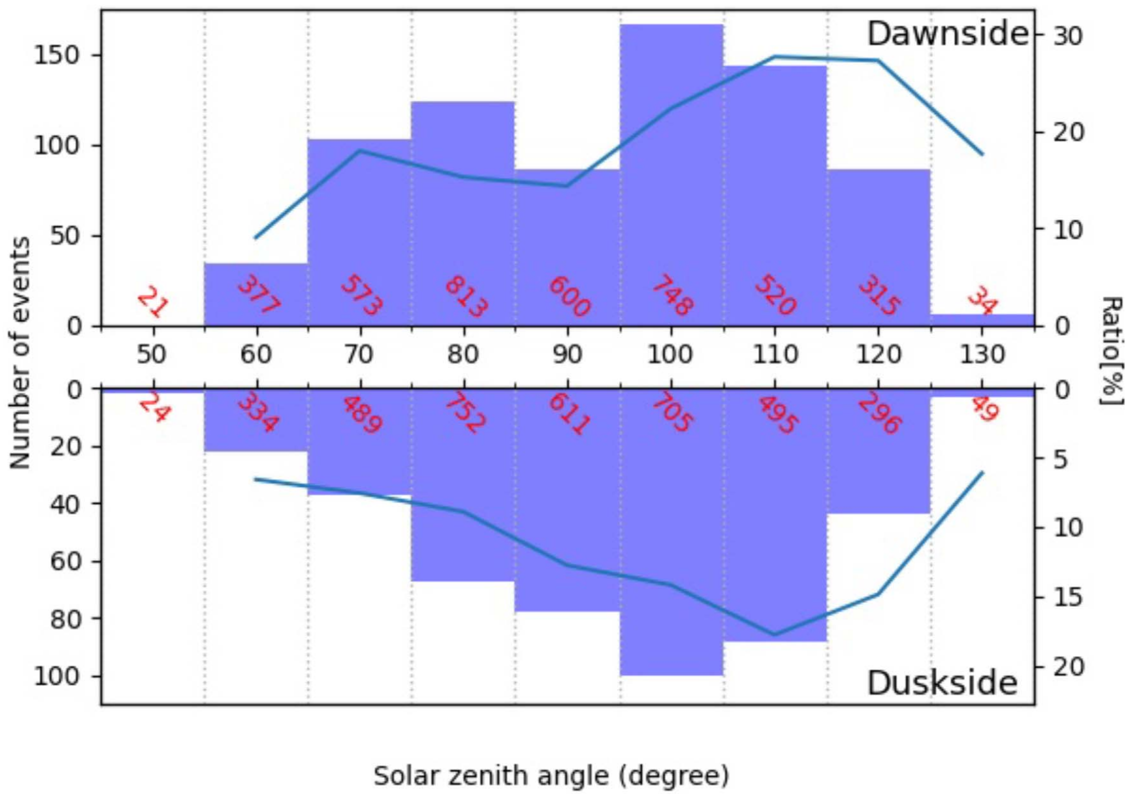

Figure 4. Histogram of the occurrence number of events (blue bars), and the occurrence ratio (light-blue line) as a function of the solar zenith angle. The red-colored numbers indicate the number of passes in each 10° bin.

ratio for the dawnside sector is about 1.7 (=20/12) times higher than the occurrence ratio for the duskside sector.

Figure 5b shows the relationship with the B_Y component. For the duskside sector (lower panel), there is no significant trend in the range from −5 nT to 5 nT with ratios of 10% to 15%. On the other hand, for the dawnside sector (upper panel), when B_Y is negative, the values range from 20% to 25%, indicating a B_Y asymmetry. To put it another way, the dawn-dusk asymmetry of the occurrence ratio is pronounced when B_Y is negative. This asymmetry will be discussed later. Figure 5c shows the relationship with the B_Z component. In the duskside sector, as shown by Yokoyama et al. (2021), there is a tendency for the occurrence ratio to increase as B_Z becomes more positive. A similar trend can be seen for the distribution for the dawnside event, with occurrence ratio exceeding 30% at B_Z of 2–3 nT. Note that the distribution with a peak at $B_Z \sim 0$ in each sector (blue bars) simply reflects the average characteristics of IMF (e.g., see Fig. 15c in Lee et al., 2009).

Figure 6 shows the relations of the current density of the mesoscale FAC to the solar wind proton density. Each blue dot represents the current density of the event, estimated with the method used by Yokoyama et al. (2021). The black dots indicate the average value for each range on the abscissa, divided into 4 cm^{-3} intervals (0–4, 4–8, 8–12, …, 24–28), and the error bars are also shown. Note that for the ranges above 28 cm^{-3}, the mean values and error bars are not plotted due to the small number of events in each range. The current density in the dawnside sector tends to increase as the solar wind proton density increases (left panels in Fig. 6). Similar tendency can be seen for the duskside sector (right panels), as was shown in Yokoyama et al. (2021).

3.5 Seasonal dependence

Figure 7 shows the seasonal distribution of the occurrence number of events and the occurrence ratio. Spring, Summer, Autumn, and Winter on the hozizontal axis represent the three-month period of February–April, May–July, August–October, and November–January, respectively. For each season, the occurrence ratio (light-blue line in Fig. 7) is higher in the dawnside sector than in the duskside sector. The feature that the occurrence ratio is higher in the dawnside sector than in the duskside sector, described in Figure 5a, is confirmed to be true for each season. A common characteristic of both sectors is that the occurrence ratio is lowest in Summer, at least 35% higher in both Spring and Autumn than in Summer, and highest in Winter. This tendency will be discussed later.

4. Discussion

4.1 Common characteristics of the dawnside and duskside events

As shown in Section 3, we analyzed the magnetic perturbation data obtained during a period of about 4 years, from January 2017 to December 2020. This period differs significantly from that examined by Yokoyama et al. (2021),

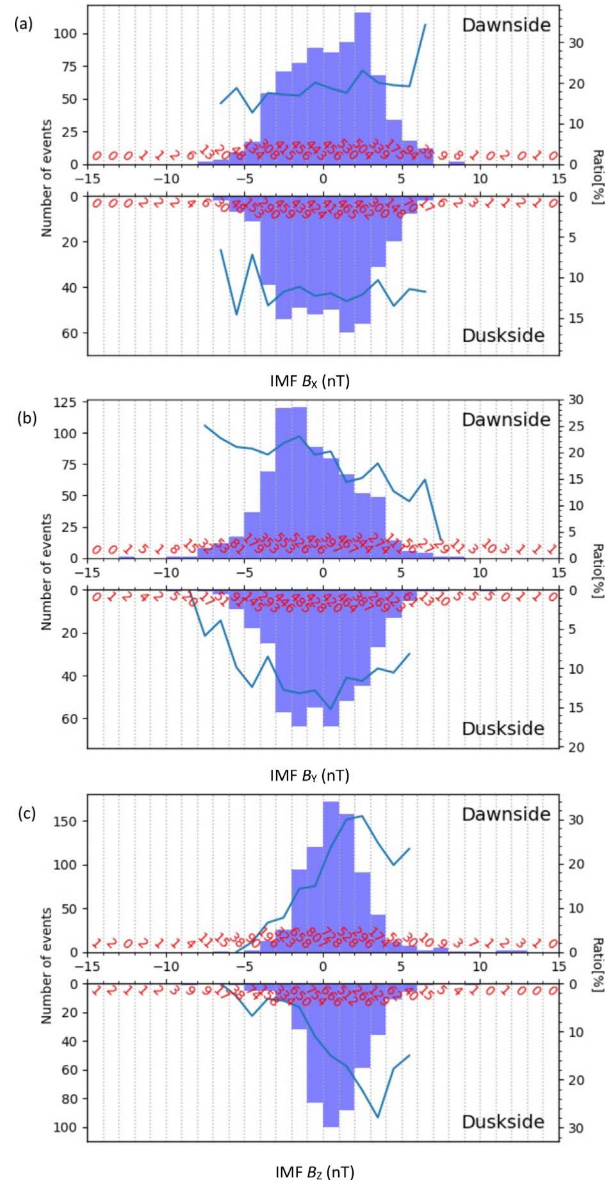

Figure 5. Histogram of the occurrence number of events (blue bars) and the occurrence ratio (light-blue line) as a function of three components of IMF: (a) *X*, (b) *Y*, and (c) *Z* components from top to bottom, respectively. The red-colored numbers indicate the number of passes in each bin.

overlapping by only about 5 months. Based on data from a period of time that differs significantly from that examined in the previous study, the following results have been obtained in this study for the duskside mesoscale FACs:

1. The latitudinal size of the upward/downward FAC is typically less than 40 km.
2. The FACs are observed both in the sunlit ionosphere and in the dark ionosphere.
3. The occurrence ratio is relatively high when IMF B_Z is positive.
4. The current density tends to increase with increasing solar wind proton density.
5. The occurrence ratio is lowest in Summer, and both ratios in Spring and Fall are at least 35% higher than that in Summer. Winter has the highest occurrence ratio.

Features 1–4 are in agreement with those obtained by Yokoyama et al. (2021), indicating that the mesoscale FACs in the duskside sector can occur at any time over a long period of time, from 2014 to 2020, if the conditions for their occurrence are met. Feature 5 was not investigated in Yokoyama et al. (2021) and is a newly found feature in this study.

Features 1–5 above are also characteristics for the dawnside mesoscale FAC. The similarity between the FAC in the dawnside sector and that in the duskside sector implies that the mechanism proposed by Yokoyama et al. (2021) for the generation of the FACs in the duskside sector is also working for the FACs in the dawnside sector. Yokoyama et al. (2021) suggested that the generation of the FAC involves the reconnection of the magnetic field lines once opened by the reconnection generated inside the Kelvin Helmholtz (KH) vortex at the magnetopause and that those field lines are reconnected again, forming closed magnetic field lines in LLBL. Indeed, Faganello et al. (2014) also pointed out that such reconnection can occur on the magnetopause. Given that the geometry of the magnetic field lines extending to the LLBL does not have any particular dawn-dusk asymmetry, the above generation mechanism may be considered to occur in the dawnside magnetopause as well as in the duskside magnetopause.

Recently, Kavosi et al. (2023) have reported the seasonal variations in the occurrence ratio of the KH instability by examining data from satellite crossing the flank magnetopause. The ratio is high in Spring and Autumn, and low in Summer and Winter. Feature 5, mentioned above, seems to be consistent with this tendency except that the occurrence ratio of the mesoscale FACs is high in Winter. If we assume that a yet unspecified mechanism is working so that the occurrence ratio of the mesoscale FACs can increase in Winter, the fact that both occurrence ratios show a similar trend except in Winter would support the suggestion by Yokoyama et al. (2021) about the generation mechanism of the mesoscale FACs, that is, the mesoscale FAC being related to the reconnection generated inside the KH vortex. Further studies are needed to identify the mechanism that explains the high occurrence ratio in Winter.

4.2 Differences in the occurrence of the dawnside and duskside FACs

Regarding the occurrence ratio of the mesoscale FAC events, there is a marked difference between the dawnside and duskside sectors. The occurrence ratio in the dawnside sector can be estimated to be about 1.7 times higher than that in the duskside sector (Fig. 5). Considering the inferred generation of the FACs mentioned above and the result shown in Figure 5b, this dawn–dusk difference in the occurrence ratio may be caused by the imbalance in which the FAC event dataset for the dawnside sector for negative IMF B_Y contains more events obtained under conditions where the KH instability is more unstable.

It has been pointed out by Nykyri (2013) that the KH instability is more likely to occur in the dawnside magnetopause than in the duskside magnetopause because the IMF is statistically more likely to be in the Parker spiral configuration. Also, based

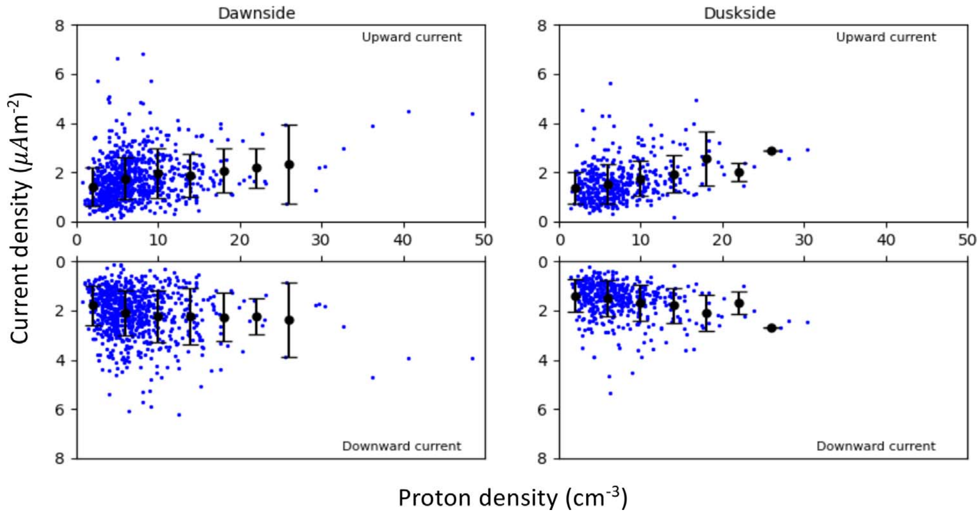

Figure 6. Scatter plot of the current density of the upward (upper panels) and downward (bottom panels) FACs as a function of the solar wind proton density. The solid black dots represent the mean values, and the error bars are ± one standard deviation for the range of <28 cm^{-3}.

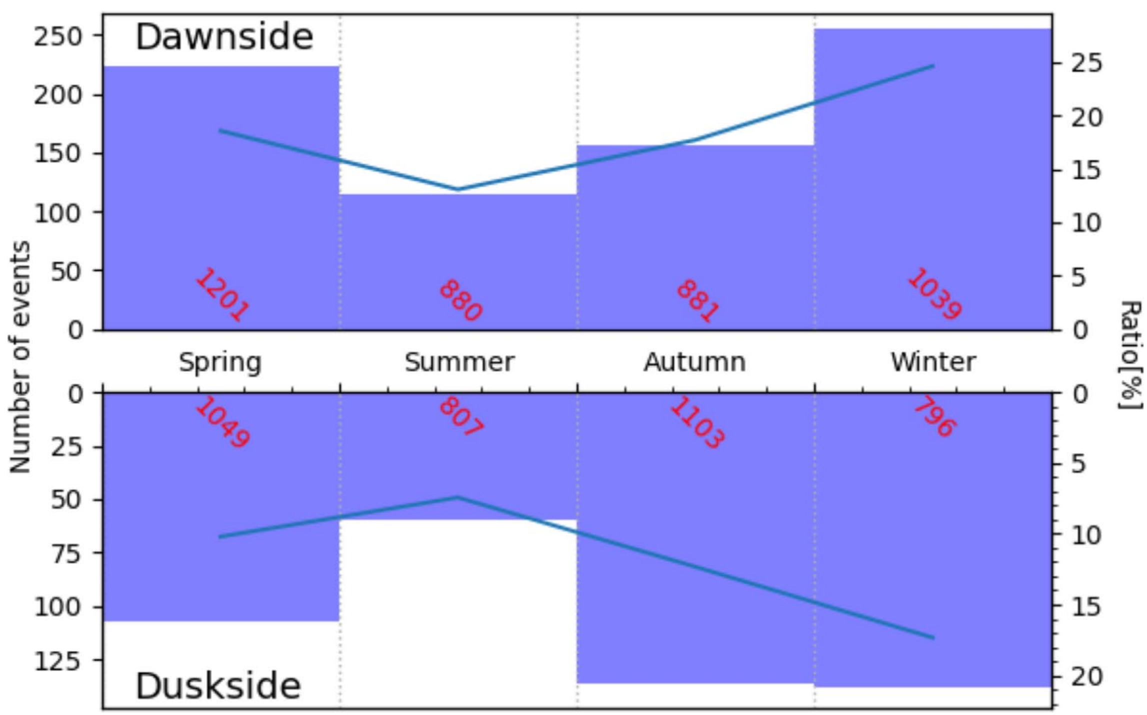

Figure 7. Seasonal distribution of the occurrence number of events (blue bars), and the occurrence ratio (light-blue line). The red-colored numbers indicate the number of trajectories in each season.

on a statistical survey of the occurrence of KH instabilities on the magnetopause based on the THEMIS satellite observations from 2007 to 2013, Henry et al. (2017) reported that KH instabilities are clearly more likely to occur under the Parker spiral IMF in the dawnside magnetopause.

We examined if more dawnside mesoscale FAC events in our dataset were obtained when IMF had a Parker spiral configuration. Figure 8 shows the results for the occurrence of the dawnside FAC events classified by the IMF angle together with the result for the duskside FAC events. We examined here the cases when IMF had a positive B_Z component. Figure 8a shows the occurrence ratio of the mesoscale FAC events in the dawnside (solid line) and duskside (dotted line) sectors against the IMF inclination angle in the X–Y plane in the GSM coordinate. A negative angle means that the IMF B_Y is negative. It can be seen that in the negative angles the occurrence ratio of the dawnside event is higher than that of the duskside event. This is consistent with the result shown in Figure 5b.

In Figure 8a the angle around $-45°$ (or $135°$) means that the IMF has a typical Parker Spiral configuration assuming that the

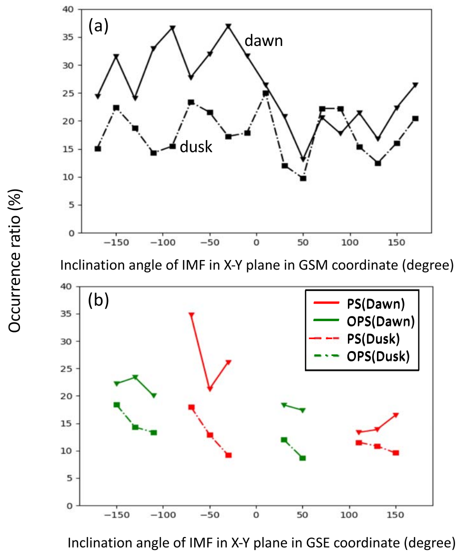

Figure 8. (a) The occurrence ratio of mesoscale FAC events in the dawnside (solid line) and duskside (dotted line) sectors against the IMF inclination angle in the *X*–*Y* plane in the GSM coordinate. An angle of zero indicates the sunward direction, and a negative angle means that the IMF has a negative B_Y component. (b) The occurrence ratio of mesoscale FAC events in the dawnside (solid line) and duskside (dotted line) sectors for the Parker Spiral configuration (red) and Ortho-Parker Spiral configuration (green) of IMF against IMF inclination angle in *X*–*Y* plane in the GSE coordinate.

angle in the GSM coordinate is not significantly different from the angle in the GSE coordinate (A Parker Spiral configuration should be evaluated in the GSE coordinate system, as will be shown later). Similarly, the angle around 45° (or −135°) means that the IMF is oriented orthogonally to the typical Parker Spiral configuration in the *X*–*Y* plane. This is referred to as the Ortho-Parker Spiral configuration. We need to know whether or not there are more cases where the angle of the IMF in the *X*–*Y* plane is around −45° in the dawnside event dataset and there are fewer cases where the angle of the IMF in the *X*–*Y* plane is around −135° in the dawnside event dataset.

Figure 8b shows the occurrence ratio of events in the dawnside (solid line) and duskside (dotted line) sectors for the Parker Spiral configuration (red) and Ortho-Parker Spiral configuration (green) cases against the IMF inclination angle in the *X*–*Y* plane in the GSE coordinate. We used the criteria adopted by Dimmock et al. (2015) for the definition of the Parker Spiral and Ortho-Parker Spiral. Specifically, we required that $B_X > 0.3\ B_T$ and $B_Y < -0.3\ B_T$ or $B_X < -0.3\ B_T$ and $B_Y > 0.3\ B_T$ for the Parker Spiral, and that $B_X > 0.3\ B_T$ and $B_Y > 0.3\ B_T$ or $B_X < -0.3\ B_T$ and $B_Y < -0.3\ B_T$ for the Ortho-Parker Spiral. Here, B_T represents the magnitude the IMF.

We understand from Figure 8b that while the dawnside events are observed most often around −70° (slightly lower than the typical Parker Spiral angle of −45°), which is one of the two ranges of the Parker Spiral configuration, more frequent occurrence in the dawnside sector than in the duskside sector is also identified when the IMF has the Ortho-Parker Spiral configuration, i.e., the angles of −150° to −110°. Considering these results, we infer that more dawnside mesoscale FAC events in our dataset may be obtained when IMF had a Parker Spiral configuration, but that is not the only reason why the dawnside event is more frequently identified than the duskside event.

Although we do not present the definitive reason for the more frequent occurrence of the dawnside events, there is a report in the literature that is consistent with this asymmetry. Lassen & Danielson (1978) statistically examined the distribution of auroral arcs during the quiescent period from about five years of all-sky camera network observations and clarified the distribution of the sun-aligned auroral arcs. Their result shows that for IMF $B_Y < 0$ the dawnside sun-aligned arcs (6–10 MLT) are prominently identified in the somewhat higher latitude region than 80° MLAT, while the duskside sun-aligned arcs (14–18 MLT) for IMF $B_Y > 0$ are rarely seen in similar MLAT.

In fact, for a strong northward IMF with a negative B_Y component, the dawnside electron precipitation region with highly structured electric and magnetic field fluctuations has properties indicating that the source is a distant LLBL (Taguchi et al. 1995). The dawnside sun-aligned arcs for IMF $B_Y < 0$ which were investigated by Lassen & Danielson (1978) may be a phenomenon with the mesoscale magnetic perturbations such as those investigated in the present study, although the horizontal size discussed by Taguchi et al., (1995) is slightly larger than the latitudinal size obtained in the present study.

As the dawn and dusk sectors of the auroral oval expand into the polar region, the polar cap can become teardrop-shaped, forming horse collar aurora (Hones et al., 1989). A recent report on horse collar aurora examines the formation and motion of 11 aurora events observed by Defense Meteorological Satellite Program satellite and an all-sky imager during the period of October 2014 through December 2016 (Bower et al., 2023). We checked the duskside mesoscale FAC events collected in Yokoyama et al., (2021) during May 2014–May 2017, which includes 11 periods that Bower et al., (2023) investigated (their Table 1), and found that the duskside mesoscale FACs were observed in 4 of the 11 periods. Although further studies are needed, the magnetospheric conditions that generate the mesoscale FACs of interest might be related to the formation of horse collar aurora.

5 Conclusions

By analyzing magnetic field data obtained by Swarm satellites at 6–10 MLT and 14–18 MLT over a four-year period from January 2017 to December 2020, we statistically investigated the similarities and differences between the dawnside mesoscale FACs and the duskside mesoscale FACs. The results of the statistical analysis can be summarized as follows:

1. The latitudinal size of the mesoscale FACs in the dawnside sector is similar to that of the duskside mesoscale FACs, and both are typically less than 40 km.
2. The mesoscale FACs in the dawnside sector occur both in the sunlit ionosphere and in the dark ionosphere. In addition, the dawnside mesoscale FACs, as well as the duskside FACs, have a relatively high occurrence ratio when the IMF B_Z is positive.
3. The current density of the FAC tends to increase with increasing solar wind proton density, which is similar to the tendency for the mesoscale FAC in the duskside sector.

4. For the mesoscale FACs in either sector, the occurrence ratio is lowest in Summer, and both ratios in Spring and Autumn are at least 35% higher than that in Summer. Winter has the highest occurrence ratio.
5. The overall occurrence ratio of the dawnside FACs is approximately 1.7 times higher than that of the duskside FACs. The more frequent occurrence in the dawnside sector may be related to the fact that KH instabilities are more likely to occur at the magnetopause on the dawnside during the Parker Spiral configuration of IMF, but further studies are needed to determine the definitive reason for the more frequent occurrence in the dawnside sector than in the duskside sector.

Acknowledgements

The work by S. Taguchi is supported in part by JSPS KAKENHI Grant Number 22H01285. The editor thanks Chao Xiong and an anonymous reviewer for their assistance in evaluating this paper.

Data availability statement

Swarm magnetometer data and current density data were obtained through the ESA Swarm website (https://swarm-diss.eo.esa.int/). OMNI solar wind data were obtained through NASA/OMNIWeb (https://omniweb.gsfc.nasa.gov/form/omni_min.html).

References

Borgogno D, Califano F, Faganello M, Pegoraro F. 2015. Double-reconnected magnetic structures driven by Kelvin-Helmholtz vortices at the Earth's magnetosphere. *Phys Plasmas* **22(3)**: 032301. https://doi.org/10.1063/1.4913578.

Bower GE, Milan SE, Paxton LJ, Spanswick E, Hairston MR. 2023. Formation and motion of horse collar aurora events. *J Geophys Res Space Phys* **128**: e2022JA031105. https://doi.org/10.1029/2022JA031105.

Dimmock AP, Osmane A, Pulkkinen TI, Nykyri K. 2015. A statistical study of the dawn-dusk asymmetry of ion temperature anisotropy and mirror mode occurrence in the terrestrial dayside magnetosheath using THEMIS data. *J Geophys Res Space Phys* **120**: 5489–5503. https://doi.org/10.1002/2015JA021192.

Faganello M, Califano F, Pegoraro F, Retinò A. 2014. Kelvin-Helmholtz vortices and double mid-latitude reconnection at the Earth's magnetopause: Comparison between observations and simulations. *Europhys Lett* **107(1)**: 19001. https://doi.org/10.1209/0295-5075/107/19001.

Friis-Christensen E, Lühr H, Hulot G. 2006. Swarm: a constellation to study the Earth's magnetic field. *Earth Planets Space* **58(4)**: 351–358. https://doi.org/10.1186/BF03351933

Gjerloev JW, Ohtani S, Iijima T, Anderson B, Slavin J, Le G. 2011. Characteristics of the terrestrial field-aligned current system. *Ann Geophys* **29(19)**: 1713–1729. https://doi.org/10.5194/angeo-29-1713-2011.

Henry ZW, Nykyri K, Moore TW, Dimmock AP, Ma X. 2017. On the dawn-dusk asymmetry of the Kelvin-Helmholtz instability between 2007 and 2013. *J Geophys Res Space Phys* **122**: 11888–11900. https://doi.org/10.1002/2017JA024548.

Hones EW Jr, Craven JD, Frank LA, Evans DS, Newell PT. 1989. The horse-collar aurora: a frequent pattern of the aurora in quiet times. *Geophys Res Lett* **16**: 37.

Kavosi S, Raeder J, Johnson JR, Nykyri K, Farrugia CJ. 2023. Seasonal and diurnal variations of Kelvin-Helmholtz Instability at terrestrial magnetopause. *Nat Commun* **14**: 2513. https://doi.org/10.1038/s41467-023-37485-x.

Lassen K, Danielson C. 1978. Quiet time pattern of auroral arcs for different directions of the interplanetary magnetic field in the *y*-*z* plane. *J Geophys Res* **83**: 5277–5284. https://doi.org/10.1029/JA083iA11p05277.

Lee CO, Luhmann JG, Odstrcil D, MacNeice PJ, de Pater I, Riley P, Arge CN. 2009. The solar wind at 1 AU during the declining phase of solar cycle 23: Comparison of 3D numerical model results with observations. *Sol Physics* **254**: 155–183. https://doi.org/10.1007/s11207-008-9280-y.

Lühr H, Park J, Gjerloev JW, Rauberg J, Michaelis I, Merayo JMG, Brauer P. 2015. Field-aligned currents' scale analysis performed with the Swarm constellation. *Geophys Res Lett* **42(1)**: 1–8. https://doi.org/10.1002/2014GL062453.

Nykyri K. 2013. Impact of MHD shock physics on magnetosheath asymmetry and Kelvin-Helmholtz instability. *J Geophys Res Space Phys* **118**: 5068–5081. https://doi.org/10.1002/jgra.50499.

Olsen N, Friis-Christensen E, Floberghagen R, Alken P, Beggan CD, et al. 2013. The Swarm Satellite Constellation Application and Research Facility (SCARF) and Swarm data products. *Earth Planet Space* **65(11)**: 1189–1200. https://doi.org/10.5047/eps.2013.07.001.

Ritter P, Lühr H, Rauberg J. 2013. Determining field-aligned currents with the Swarm constellation mission. *Earth Planet Space* **65**: 1285–1294. https://doi.org/10.5047/eps.2013.09.006.

Taguchi S, Sugiura M, Iyemori T, Winningham JD, Slavin JA. 1995. Highly structured ionospheric convection for northward interplanetary magnetic field: A case study with DE 2 observations. *J Geophys Res* **100(A8)**: 14743–14753. https://doi.org/10.1029/94JA03373.

Thébault E, Finlay CC, Beggan CD, et al.et al. 2015. International geomagnetic reference field: the 12th generation. *Earth Planets Space* **67**: 79. https://doi.org/10.1186/s40623-015-0028-9.

Xiong C, Lühr H. 2014. An empirical model of the auroral oval derived from CHAMP field-aligned current signatures – part 2. *Ann Geophys* **32**: 623–631. https://doi.org/10.5194/angeo-32-623-2014.

Yokoyama Y, Taguchi S, Iyemori T, Hosokawa K. 2020. The quasipersistent feature of highly structured field-aligned currents in the duskside auroral oval: Conjugate observation via Swarm satellites and a ground all-sky imager. *J Geophys Res Space Phys* **125**: e2019JA027594. https://doi.org/10.1029/2019JA027594.

Yokoyama Y, Taguchi S, Iyemori T. 2021. Importance of the northward IMF for the quasistatic mesoscale field-aligned currents embedded in the diminished Region 1/2 current system in the dusk sector. *J Geophys Res Space Phys* **126**: e2020JA028774. https://doi.org/10.1029/2020JA028774.

Cite this article as: Yokoyama Y & Taguchi S. 2024. The nature of the mesoscale field-aligned currents in the auroral oval for positive IMF B_Z: More frequent occurrence in the dawnside sector than in the duskside sector. *J. Space Weather Space Clim.* **14**, 16. https://doi.org/10.1051/swsc/2024013.